J. Micromech. Microeng. **23** (2013) 125014 (10pp) doi:10.1088/0960-1317/23/12/125014

Optimization of nanofountain probe microfabrication enables large-scale nanopatterning

Asmahan Safi[1], **Wonmo Kang**[1,2], **David Czapleski**[3], **Ralu Divan**[3], **Nicolae Moldovan**[2] **and Horacio D Espinosa**[1,2]

[1] Department of Mechanical Engineering, Northwestern University, 2145 Sheridan Rd., Evanston, IL 60202, USA
[2] iNfinitesimal LLC, 559 Arbor Vitae Rd, Winnetka, IL 60093, USA
[3] Center for Nanoscale Material, Argonne National Laboratories, 970 S. Cass Ave., Building 440, Argonne, IL 60439, USA

E-mail: espinosa@northwestern.edu

Received 9 May 2013, in final form 14 August 2013
Published 11 November 2013
Online at stacks.iop.org/JMM/23/125014

Abstract
A technological gap in nanomanufacturing has prevented the translation of many nanomaterial discoveries into real-world commercialized products. Bridging this gap requires a paradigm shift in methods for fabricating nanoscale devices in a reliable and repeatable fashion. Here we present the optimized fabrication of a robust and scalable nanoscale delivery platform, the nanofountain probe (NFP), for parallel direct-write of functional materials. Microfabrication of a new generation of NFP was realized with the aim of increasing the uniformity of the device structure. Optimized probe geometry was integrated into the design and fabrication process by modifying the precursor mask dimensions and by using an isotropic selective dry etching of the outer shell that defines the protrusion area. Probes with well-conserved sharp tips and controlled protrusion lengths were obtained. Sealing effectiveness of the channels was optimized. A conformal tetraethyl orthosilicate based oxide layer increased the sealing efficacy while minimizing the required thickness. A compensation scheme based on the residual stresses in each layer was implemented to minimize bending of the cantilever after releasing the device. The device was tested by patterning ferritin catalyst arrays on silicon dioxide with sub-100 nm resolution. The optimized probes increased the control over the parallel patterning resolution which enables manufacturing of ordered arrays of nanomaterials.

S Online supplementary data available from stacks.iop.org/JMM/23/125014/mmedia

(Some figures may appear in colour only in the online journal)

1. Introduction

Tip-based nanofabrication (TBN) has established itself over the past decade as a powerful technique for patterning a diverse range of nanomaterials [1–4]. The spatial accuracy of scanning probe-based systems provides the control necessary for repeatable assembly in the 10 to 1000 nm range in a reproducible manner. Conventional CMOS fabrication techniques have demonstrated nanoscale structures but at an ever increasing cost [7]. TBN, along with template-based approaches such as nanoimprint lithography, is one of the primary techniques benefitting the development and prototyping of nanodevices by making nanopatterning possible with reasonable-cost equipment and in small lab facilities [5, 6]. At the same time, other fabrication techniques have not been able to address the critical challenges of nanomanufacturing [5] that must be met for a nanofabrication or assembling technique to be economically viable: (1) control of the size, position orientation and properties of materials at the nanoscale; (2) multi-scale integration and interfacing

 © 2013 IOP Publishing Ltd Printed in the UK & the USA

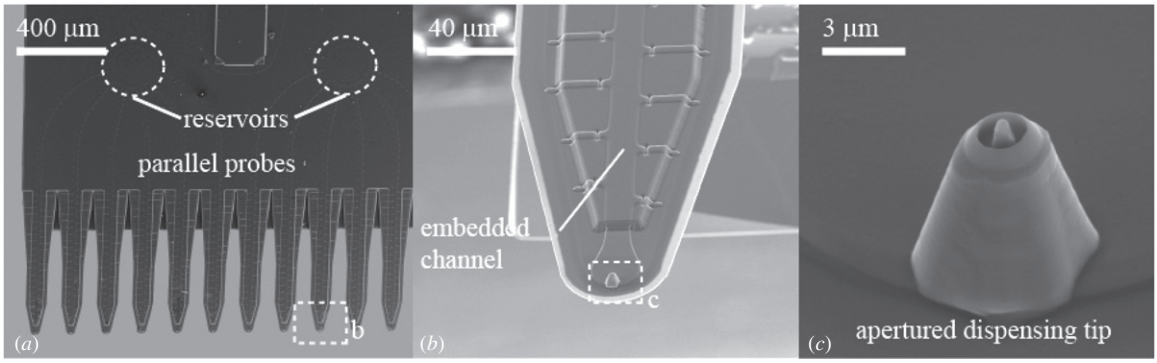

Figure 1. SEM images of the fourth generation NFP. The NFP chip consists of four reservoirs (*a*) that are each connected to six parallel microfluidic cantilevers. The reservoir membrane distributes the ink into the embedded microfluidic channels (*b*), which deliver the ink to the writing probe tips (*c*).

with the 'device architecture'; (3) scalability for large-scale production; and (4) robustness and reproducibility for a reasonable cost [5]. Addressing these challenges will enable the transition of nanotechnology discoveries from laboratory benches to consumer markets [6, 8, 9] in fields ranging from nanoelectronics, nanomedicine [10], defense to energy storage [11, 12]. Similar to e-beam patterning, TBN has a weak point in the slow speed of patterning, which can be addressed in part by parallel patterning with arrays of tips. The approach demonstrated here addresses this problem by using a linear array of 12 probes.

The nanofountain probe (NFP) is a device with integrated microfluidic channels that enables high throughput bottom–up direct-write patterning [13, 14]. NFP has been used to pattern DNA [15], proteins [16], gold [17] and diamond nanoparticles [18] with sub-100 nm resolution. The NFP operates as a miniaturized fountain pen such that an 'ink' containing material in aqueous suspension is loaded into the reservoir (supporting information available at stacks.iop.org/JMM/23/125014/mmedia) and delivered by capillary forces to an aperture probe tip via an embedded channel in the cantilever body (figure 1). When the sharp apex of the probe contacts a substrate, a meniscus forms and the liquid is then deposited and diffuses on the substrate surface. Analysis shows that the size of the meniscus is a strong function of the probe protrusion [16].

NFP patterning is a scanning-based method allowing both top–down and bottom–up fabrication. The integrated microfluidic reservoir and channels allow ink material to stay in a hydrated state through the entire delivery process from inking to patterning stages. This unique NFP feature allows the NFP to operate submerged in both air and liquid environments [19]. It shares similar capabilities with dip-pen lithography [20, 21] (DPN) in term of resolution and registration but also its serial limitations. Nevertheless, successful DPN patterning using 55 000 pen arrays [22] at an estimated 0.05 cm^2 min^{-1} rate demonstrated the method's scalability. An NFP patterning rate of 2.66×10^{-6} cm^2 min^{-1} was measured in this work. Operation in parallel along with on-going fast-scan AFM development promises to increase the throughput toward large-scale nanomanufacturing. Along with the integrated continuous molecular feeding, a current parallelization scheme, consisting of two 1D arrays of 12 cantilevers integrated on a single chip, allows maskless parallel fabrication of extensive patterned areas in a single pass and reduced process time by eliminating molecular loading steps and ink kinetic dissolution at the tip meniscus [23]. Scaling-up schemes similar to the 2D probe array demonstrated with DPN [22] are envisaged to increase the throughput of the NFP. In contrast, commercially available systems, such as e-beam [24, 25] (EBL) and nanoimprint lithography [24, 26] (NIL) can reach 10 nm resolution, although at very different patterning rates. EBL is also a serial method with reported rates up to 0.001 cm^2 s^{-1}. NIL relies on embossing and thus is privileged by large-scale and faster templating capabilities but it requires a mold for each desired pattern. Step and repeat methods using NIL have reached patterning rates between 0.002 and 0.3 cm^2 s^{-1} [27]. E-beam lithography offers orders of magnitude faster patterning and is currently the best candidate to replace traditional lithography for semiconductor industry. The scanning probe-based patterning such as DPN and NFP on the other hand allow patterning of a library of materials that cannot be patterned directly by EBL such as proteins, nanoparticles and biomolecules. Furthermore, the integrated microfluidic delivery of the NFP enables patterning of materials that require delivery in a hydrated state.

In this paper, we present the approach taken to increase the throughput and resolution obtained by NFP patterning. The following sections present the design and fabrication process of the fourth generation of NFP. Using knowledge from the fabrication and use of the previous generation devices [14, 28], the probe geometry was redesigned and the fabrication process was adapted to increase uniformity across the wafer, while improving the probe profile, and to increase the resolution and performance for parallel patterning applications. We discuss modifications to the dispensing probe, including sealing of the microfluidic channels and beam stress compensation to avoid residual probe curvature. Characterization of the device, including the probe geometry, cantilever bending and stiffness, are then presented. Application of the device is demonstrated by patterning arrays of catalyst nanomaterials.

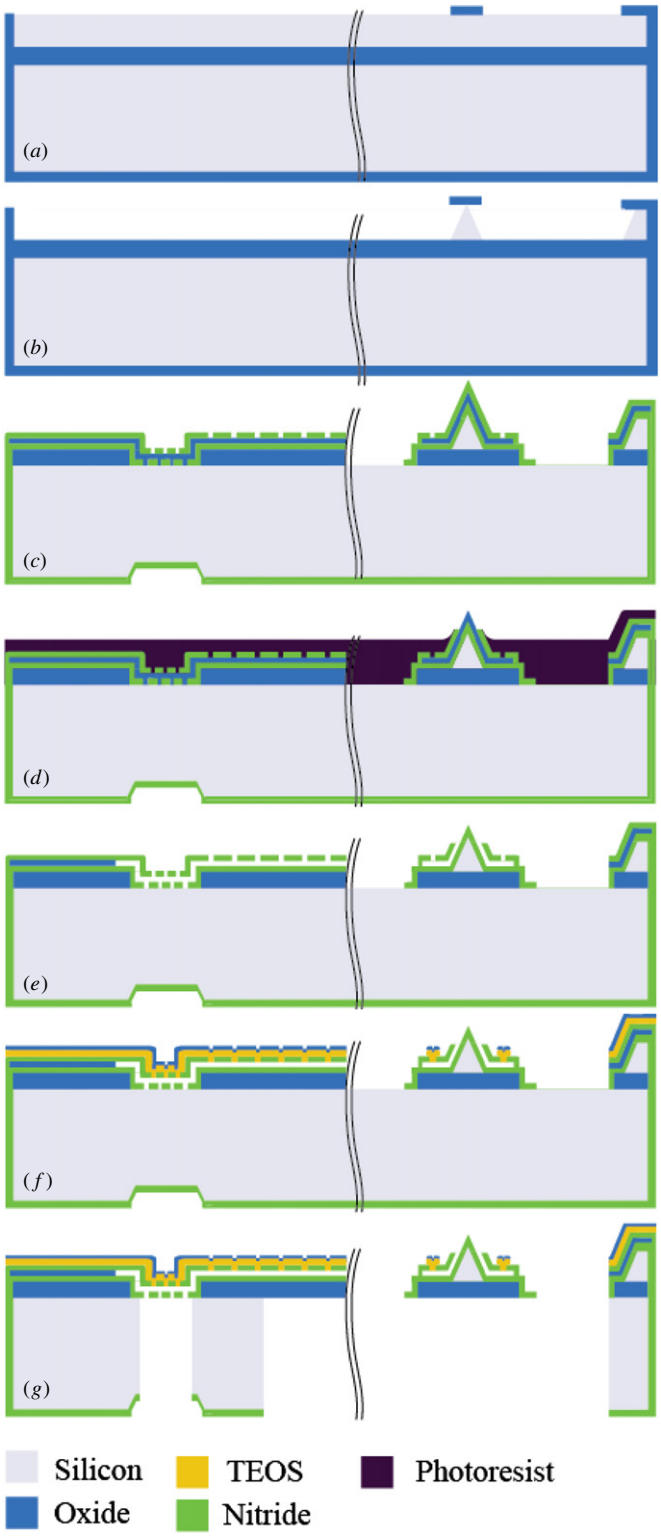

Figure 2. Illustration of the fabrication process: (*a*) Mask precursor patterning; (*b*) definition of sharp silicon tips; (*c*) successive deposition, lithography and patterning to form the channel core and the envelope; (*d*) definition of the dispensing tip by locally etching the probe outer shell; (*e*) release of the channel; (*f*) sealing of the side channels; (*g*) reservoir and chip body definition.

2. Fabrication

The fabrication process, shown in figure 2, consists of three major steps for delineating: the volcano-shaped tips, the microchannels, and the chip body with reservoir area. The process begins with the formation of sharp silicon tips onto silicon on insulator (SOI) wafers. A masking layer of thermal oxide is grown (∼200 nm thick), followed by lithography and dry etching on the front side to form the tip precursor mask (figure 2(*a*)). Then, silicon tips are created by wet anisotropic etching of the device layer in 40% wt. tetramethyl ammonium hydroxide (TMAH) (figure 2(*b*)). Sharp tips are formed by fast etch planes appearing through convex corner undercutting of the thermal oxide mask [29].

The fabrication of microfluidics-embedding cantilevers is realized by successive deposition, lithography and etching of the layers composing the channels (figure 2(*c*)). First, the cantilever body is outlined in the buried oxide. The SiO_2 is patterned using a thick ∼9.5 μm photoresist (SPR220-7) then defined by wet isotropic etching in buffered oxide etch (BOE). A post-exposure bake of the resist increases the adhesion and limits the diffusion of fluoride ions through the photoresist mask. The bulk part of the cantilever is fabricated as in previous generations [28], a summary of which follows. A layer of low stress silicon nitride (∼380 nm thick) is deposited by low pressure chemical vapor deposition (LPCVD). The channel floor is formed through contact lithography of the Si_3N_4 using Shipley 1813 spun at 3000 rpm and patterning by CHF_3+O_2 reactive ion etching (RIE) (Oxford Plasmalab 100, Oxfordshire, UK). The sacrificial core of the channel is formed by depositing a 500 nm silicon dioxide by plasma-enhanced chemical vapor deposition (PECVD) (GSI) and patterning using buffered oxide etch BOE, using the same lithography procedure used for the buried oxide. Finally, a second low-stress silicon nitride (∼750 nm) layer is deposited by LPCVD. Subsequently, the ceiling of the channels and access holes are patterned using Shipley 1813 spun at 3000 rpm s^{-1} and CHF_3:O_2 RIE.

The outer shell of the volcano dispensing tip is formed by removing the nitride layer from the tip apex. For this, a thick SPR220-3 photoresist is spun over the wafer at spinning speed of 1000 and 1250 rpm leaving the tips protruding out of the resist by approximately 0.4 to 1 μm (figure 2(*d*)). The exposed nitride is etched by inductive coupled plasma reactive ion etching (ICP-RIE) etch (Oxford Plasmalab 100) using a 50:2 sccm mix of CHF_3:O_2 gases at 40 mTorr with ICP and RIE power of 1500 and 110 W, respectively. After removing the residual photoresist, the channels are released by etching the sacrificial PECVD oxide in BOE (1:6) for 400 min (figure 2(*e*)). A critical point dry follows to avoid collapsing the channel due to capillary forces during drying. The channels are sealed by covering them with a 2.8 μm oxide layer (figure 2(*f*)). Tetraethyl orthosilicate (TEOS)-based oxide is deposited for this purpose by PECVD at 365 °C followed by an additional 450 nm thick layer of undoped oxide deposited at 400 °C to balance the stress in the cantilever.

At last, the reservoir and chip body are defined by deep reactive ion etch (DRIE, STS LX Pegasus) using a commercial Bosch process (figure 2(*g*)). Trapezoidal trenches 40 μm deep are etched in TMAH solution beforehand at the location of the reservoir well. The recess compensates a micro-loading effect, causing a difference in etch rate between the chip body

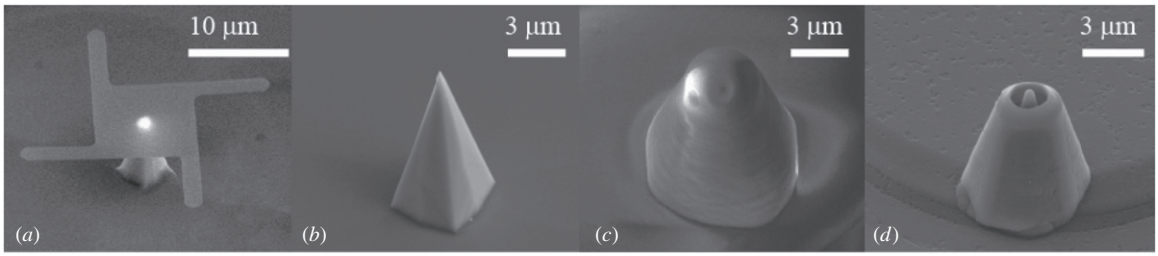

Figure 3. SEM images illustrating evolution of the probe during fabrication. (*a*) Probe precursor mask with corner compensation beams used to define pyramidal tips by anisotropic wet etch; (*b*) sharp silicon tip resulting after etch once the precursor mask is removed; (*c*) tip covered by three nitride layers that form the microfluidic structure; (*d*) the dispensing probe, with an inner tip protruding from the outer shell, that forms after the nitride layer is partially etched.

and reservoir. Wafers are handle-bonded on a support wafer using thermal paste (Cool-Grease CGR7016, AI Technology Inc.) to lengthen the etch after the first punch-through event due to non-uniform etching. The DRIE etch is carried out until all of the double nitride membranes in the reservoir well are visible. Finally, wafers are de-bonded and cleaned in a piranha solution. The resulting NFPs are rinsed with deionized water and then methanol and dried on a hotplate at 150 °C before storage.

3. Results and discussion

The new design and fabrication strategies focused on controlling the geometry of the dispensing tips, improving the effectiveness of the channel sealing after release, and compensating for the residual stress in the multilayer to avoid cantilever bending after processing.

3.1. Optimization of the dispensing tips

NFP-patterning resolution is partly defined by the probe geometry. Along with the sharpness of the probes, previous models [16] suggested that the resolution could be controlled by the meniscus shape, which depends heavily on the length by which the inner tip protrudes from the outer shell. Consequently, the precursor mask was redesigned and the outer shell etching process was modified to improve the control of the probe dimensions and improve tip uniformity across the wafer.

The precursor mask dimensions are redesigned to allow the vertical etch front to reach the oxide layer before the horizontal etch front converges to a single point. The buried oxide acts as an etch-stop layer limiting the probe height to the thickness of the device layer of the SOI wafer (10 μm). This etch stop balances the etch rate variation across the wafer during the final release by DRIE and increases the tip height uniformity. The mask consists of a square mesa of side L_{mesa} with four $\langle 1\,1\,0\rangle$-oriented compensation beams (figure 3(*a*)). The length l and width w of the compensation beams are optimized to reach the required etch depth H [30, 31]:

$$H = \frac{R^{\langle 100\rangle}}{2R^{\langle 411\rangle}}\left(l + \frac{w}{2\tan\alpha} + \frac{L_{\text{mesa}}}{2}\tan\alpha\right). \quad (1)$$

The first two terms account for the depth etched by undercutting the compensation beams, while the last term accounts for undercutting the mesa. The etch-rate (R) ratio between the $\{4\,1\,1\}$ fast undercutting place at the convex corners and $\{1\,0\,0\}$ silicon wafer surface is 1.72 at the TMAH concentration used [30]. α accounts for the 30.96° angle between the $\langle 1\,1\,0\rangle$ direction of the beams and the $\langle 4\,1\,0\rangle$ direction, which correspond to a line intersecting the $\{4\,1\,1\}$ plane and the $\{1\,0\,0\}$ plane [31]. The ratio of the width of the compensation beam to the length of the main structure is kept below $\frac{1}{4}$ because wider blades lead to a decrease in apex sharpness [32]. Etch tests were carried out to verify the models and qualitatively compare the resulting tips in terms of height, sharpness and aspect ratio. Precursor caps of various dimensions were prototyped on oxidized bulk silicon wafers with a laser pattern generator (Microtech LW405, Palermo Italy). Eventually, optimal structure dimensions for L, l and w were set at 21, 16 and 3.5 μm, respectively, for 10 μm high tips. Since the structure relies on a transitional etching profile, monitoring is essential to stop the etching at the moment the etching facets meet, to preserve the tip height. The etch progression is observed on precursor caps of increasing size, placed on the device wafers as test patterns. Once the caps of largest dimensions fall off the tips, the pyramids are fully formed (figure 3(*b*)) and the wafers are removed from the etch solution.

Shaping the outer shell surrounding the core tip is a critical step that influences the patterning resolution of the NFP. First, the sharpness of the inner Si_3N_4 tip needs to be preserved throughout the process. Second, the shell-core tip protrusion length should be controlled to a certain length. Previous modeling studies investigating the flow of liquid through the probe show that protrusion length affects the patterning resolution [16]. Probes with protrusion length between 400 and 1000 nm result in a narrow and well-defined meniscus, and therefore, an optimal patterning resolution. Above this range, the meniscus is discontinuous, whereas below this range the liquid spreads to the outer shell and results in uncontrollable patterning.

The outer shell is defined by locally etching the tip apex. To form the shell opening, a thick photoresist is spun to cover all features except the apex of the tips. Spinning speeds of 1250, 1100 and 1000 rpm are used to reach protrusion lengths within the range defined by the fluid models described earlier in the paper of 400, 600 and 1000 nm, respectively. The outer

shell is plasma-etched using a fluorine mixture of CHF_3 and O_2. Its high selectivity for nitride over silicon [33] (up to 300:1) along with the isotropic etch enables the control of the protrusion length and avoids any dulling of the tip apex from over-etching. A fluorocarbon film forms during steady-state etching conditions, leaving a reaction layer at the interface with the nitride where the etching occurs [34]. Silicon surfaces lead to a much thicker fluorocarbon film, limiting the ion flux and therefore lowering the etch rate of the substrate [34]. Consequently, the outer shell is selectively etched while the geometry and sharpness of the silicon core tip is preserved.

Inductively coupled plasma (ICP) etching is used instead of simple reactive ion etching (RIE) because it can produce a selective, largely isotropic etch. Increasing the ICP source power of the high-density plasma boosts the etch rate. The higher concentration of reactive neutrals generated increases the chemical component of the etch mechanism and/or the ion flux, which increases both the bond breaking efficiency and the sputter desorption of etch products from the surface [35]. The isotropic nature of the chemical etch is also a safeguard to preserve the probe geometry while effectively removing the nitride material uncovered by photoresist. A power ratio of ICP to RIE was set at 1500:115 W. Using an RIE power above 100 W was necessary to provide a voltage bias above 100 V and overcome the byproduct passivation layer covering the nitride. Little to no etching was observed when using lower RIE powers probably due to the very low voltage bias. Previous studies evidenced a faster etch rate on inclined surfaces with increasing bias voltage [34], which indicates that etching of the nitride on the slopes of the tip proceeds faster than on the nearly vertical surfaces. Scanning electron microscope (SEM) images (figure 3(*d*)) of the probes after ICP etch and resist stripping show a well-defined outer shell with tapered edges, which denotes an isotropic etch. Furthermore, the geometry of the inner tip is preserved throughout the process.

3.2. Sealing of side channels

The oxide material used for sealing the side channels was selected beforehand by testing and imaging several deposition oxide layers. Side channels are designed with openings to allow access for wet etchant to release the main channel from the tip to the reservoir. These cavities are hermetically sealed afterward by oxide film deposition. Because uneven sealing was observed in previous NFP generations, several sealing materials were considered and tested. Oxide material was ultimately chosen for its etching selectivity with respect to the cantilever nitride materials. In the present fabrication process, PECVD oxides from silane and TEOS are sequentially deposited on the cavities. Sealing efficacy was tested incrementally by observing the flow of water from the central channel into the side beams under a stereomicroscope as described in previous work [36]. SEM cross-sections of the cavities (figure 4) show that deposition with the two silicon oxide sources results in a significant difference in film coverage and gap filling. Differences in the molecular transport mechanism lead to a distinct deposition profile. For silane-based oxide (figure 4(*a*)), growth kinetics

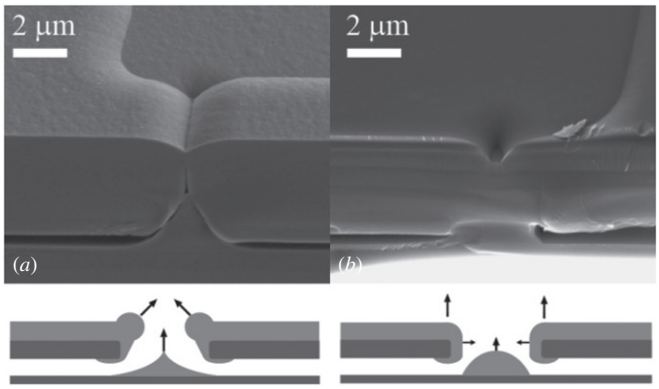

Figure 4. Sealing. SEM images and schematic illustrating the step coverage for different types of oxide deposited by PECVD. (*a*) Silane-based SiO_2 growth kinetics is favored at the edges resulting in thicker step coverage while (*b*) TEOS results in a smoother conformal film, filling the inside of the cavity as well as edges, and requiring a much lower thickness to achieve sealing than the silane-based oxide.

is highly favored at high energy surfaces such as edges [37, 38], leading to heavier deposition on the overhang and poor conformity (78% of the nominal thickness).

Sealing occurs when the deposited oxide overhangs came into contact at thicknesses of 4.7 and 4.3 μm for silane-based oxide deposited at 400 and 200 °C, respectively. TEOS-based oxide (figure 4(*b*)) deposition at 365 °C is more conformal with a bottom and sidewall coverage up to 112% of the nominal thickness. The low sticking coefficient that is characteristic of TEOS precursors results in more collisions with the walls of the structure [39], which allows TEOS to reach less accessible areas. Consequently, sealing occurs when the growth front from both sidewalls and the bottom of the cavity chemically bond. Therefore, TEOS-based oxide requires a much lower thickness of 2.8 μm to achieve a seal due to its conformality and gap filling ability, and therefore was selected as the optimal sealing material. In the end, this result demonstrates one can reduce the sealing factor, i.e. the ratio of the sealing layer thickness to the gap thickness, from 3.6 to 2.15 and improve the gap filling by selecting a deposition method with the lowest sticking coefficient.

3.3. Prevention of cantilever bending

In addition to sealing quality, the materials considered for sealing were also compared in terms of residual stress because the sealing layer can also be used to compensate for bending that occurs in the multilayered cantilever after release from the substrate. The residual stresses of oxide materials considered for sealing were characterized using the Stoney equation and the measured wafer curvature [40]. Oxide from the silane-based source deposited at 200 and 400 °C yielded 152 and 391 MPa of compressive stress, respectively. TEOS-based oxide deposited at 365 °C has 51 MPa of compressive stress. To assist in the final choice of material and thickness, bending across the length of the cantilever is predicted as a function of the sealing oxide thickness (figure 5). From Euler–Bernoulli beam theory [40], the deflection profile of a cantilever can be

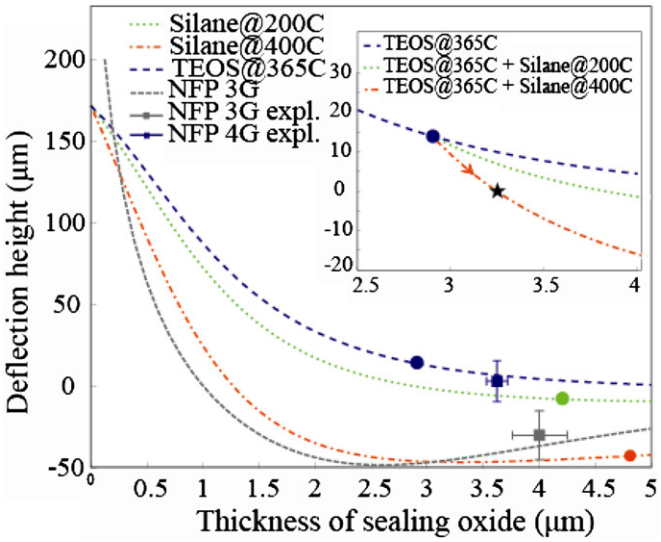

Figure 5. Bending results from residual stresses for each type of oxide. Plots of the deflection height (in μm) at the end of the cantilever for a sequence of increasing thicknesses of different PECVD oxides on a single sample: silane-based oxide deposited at 200 °C (green) and 400 °C (red) and TEOS-based oxide deposited at 365 °C (blue). TEOS was selected because of the lower thickness (2.85 μm) required for the sealing compared to the two others 4.2 and 4.9 μm. The corresponding dots represent the thickness at which a complete sealing was experimentally achieved. An additional layer of silane-based oxide was deposited at 400 °C (see inset) to balance the internal stresses of the multilayer and reach a deflection close to 0 (black star). Deflection data measured experimentally by SEM for both probes from the third and fourth generation are also plotted.

calculated by solving the following second-order differential equation for the beam curvature with appropriate boundary conditions:

$$\frac{\partial^2 u}{\partial x^2} \approx \rho = -\frac{M(x)}{EI(x)} \text{ with } u(x=0) = 0;\ \left.\frac{\partial u}{\partial x}\right|_{x=0} = 0, \quad (2)$$

where u is the deflection, ρ is the radius of curvature, M is the applied moment, E is the Young's modulus of the beam reference material, and I is the moment of inertia of beam cross-section.

The moment applied on the beam is generated by the internal stresses present in each layer according to the following equation:

$$M = \sum M_i = \int z\,\mathrm{d}F = \int_{-\frac{w_i}{2}}^{\frac{w_i}{2}} \sigma_{i_x}\,\mathrm{d}y \int_{z_i-\frac{t_i}{2}}^{z_i+\frac{t_i}{2}} z\,\mathrm{d}z, \quad (3)$$

where w_i, t_i, σ_i and z_i are the width, thickness, axial stress and distance to the neutral axis for each layer 'i', respectively. The resulting deflection height is obtained by numerically integrating the differential equation (2) twice and imposing zero displacement and no slope at the anchor of the beam.

The equivalent moment of inertia $I(x)$ is calculated using the parallel axis theorem:

$$I = \sum I_i = \sum_i \frac{w_i t_i^3}{12} + w_i(x) t_i (z_i - z_{\text{neutral}})^3, \quad (4)$$

where the equivalent neutral axis z_{neutral} is a function of x because of variations in the layer width along the cantilever length,

$$z_{\text{neutral}}(x) = \frac{1}{\sum_i w_i t_i} \int_0^{\sum t_i} w_i(x) z\,\mathrm{d}z. \quad (5)$$

Plots in figure 5 show results from numerical integration realized in Matlab that compare the evolution of the bending for an increasingly thicker layer of silane-based oxide deposited at 200 and 400 °C, TEOS-based oxide, and a porous silane-based oxide sealing layer used in previous NFP generations [14]. The experimentally measured sealing thickness for each tested layer is indicated by a dot. The thickness required for compensating the residual stresses with TEOS is larger than the minimal sealing thickness. A thin layer of silicon oxide is added over the TEOS-based oxide after sealing of the channel to achieve a near zero bending at minimal thickness (figure 5 inset). Silane-based oxide deposited at 400 °C was selected as an additional layer to minimize the total thickness and reduce the stiffness of the cantilever.

3.4. Characterization of the optimized device

The probe geometry has been characterized by SEM imaging after processing. Over 71% of the tips across the wafer were found with pyramid facets converging in a single point and radii smaller than 500 nm. These tips were categorized as sharp. Figure 3 shows an inner tip with a well-preserved sharpness. A statistical measurement of the radius of the inner tip gives on average 341 ± 68 nm. The measured radius corresponds to the thickness of the first silicon nitride covering the inner probe indicating no over-etching of the inner probe occurs during the protrusion definition. Nevertheless, the later layer reduces the sharpness of the silicon tip. Experiments show that additional dry etching of the nitride of the probe reduced its radius down to 29.3 nm (figures 6(*a*) and (*b*)). Protrusion length of 749 ± 110 and 433 ± 74 nm, respectively, are statistically measured for corresponding photoresist spinning speed of 1000 and 1250 rpm s^{-1}. Some of the measured variation inherently originates from the non-uniformity of the tip height across the wafer. Switching the fabrication method from transitional etch profile characterizing a pyramidal tip to a self-limited etch profile characterizing pyramidal pit with a subsequent molding process instead would increase the tip height uniformity.

Side-view SEM imaging of the probes showed no curvature of the cantilever. Bending is measured at 3.6 ± 11.3 μm as reported in figure 5. Variation likely comes from the over-etching of the buried oxide layer during the DRIE step. Additional measurements using a laser interferometer (Zygo NewView 7300) reveal a progressive bending along the cantilever and a flat surface near the probe (figure 6 (*c*)). No bending variation from parallel probes is detected. All cantilevers bend with standard deviation of 0.5 μm, which correspond to the range of the probe height variation itself. Unlike previous generations, no tilt is required when mounting the probes on atomic force microscope (AFM) to obtain signal from the laser reflection on the back of the cantilever to the photodetector.

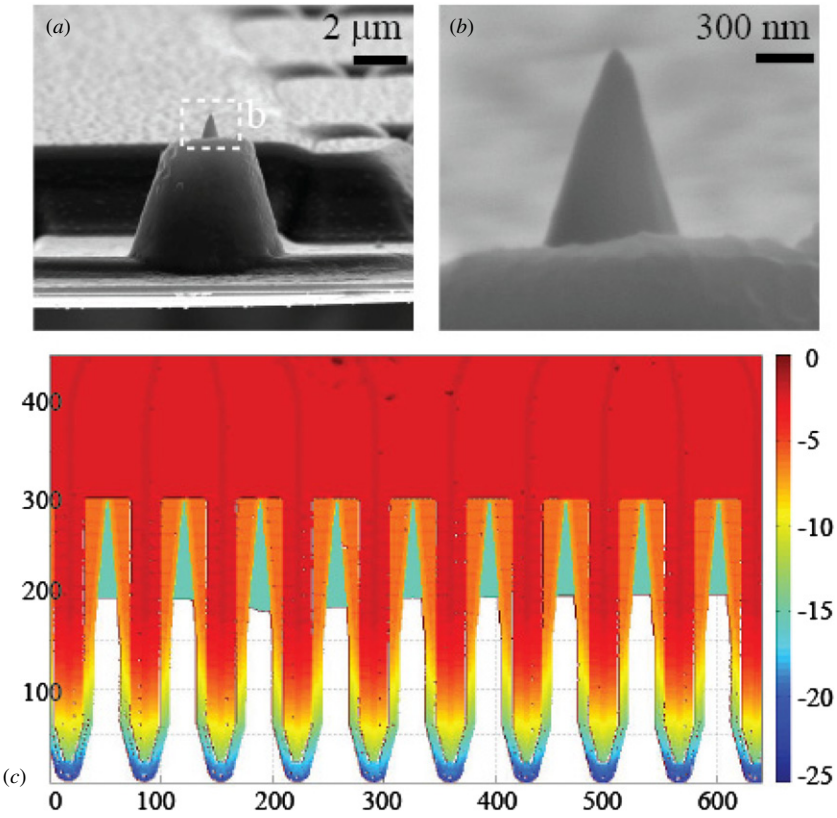

Figure 6. Characterization of NFP. (*a*, *b*) Side-view SEM imaging of probe geometry after additional dry etching. Close-up of the probe shows the inner tip protruding from the shell has retained its initial sharpness. (*c*) Map of the height of the cantilever and chip body obtained by laser interferometry in μm. Plot shows a progressive bending up to 18 μm relative to the chip body. The cantilever area where the probes sit is flat.

Finally, the stiffness of the cantilever is characterized by static deflection of reference cantilevers. The two 1D arrays of cantilevers (on opposite sides of the chip with different length) yielded 3.43 and 1.62 N/m, respectively. The additional buried oxide layer explains the rigidity of the cantilevers compared to the previously reported stiffness [28].

4. Application of device

The newly fabricated probe functionality is demonstrated by patterning arrays of ferritin catalyst. This protein ink was selected to study the patterning resolution of the new generation of NFP for sub-100 nm scale. Ferritin is a common catalyst used for carbon nanotube growth (CNT). The protein consists of a spherical shell made of 24 polypeptide subunits. The central core stores up to 4500 iron atoms in the form of ferrihydrite. The proteins have a consistent diameter of approximately 8 nm for the core and 12 nm for the shell. The protein shell prevents the nanoparticles from aggregating in solution. Clusters of larger catalyst were linked to yield significantly smaller growth yield of CNT [41].

A 0.14 mg ml^{-1} solution of ferritin protein diluted in 80% vol. water 20% vol. glycerol is loaded in the backside reservoir. The wetting of the channels from the reservoir to the tips is confirmed by observing the displacement of the meniscus in the microchannels under an optical microscope. The NFP device is then loaded in an AFM (Dimension3100 DI Instruments) and the probes are engaged on the substrate after aligning the photodetector laser on a single cantilever. Arrays of catalyst dots are patterned, on a silicon substrate with a 200 nm thermal oxide layer, under ambient conditions (25 °C and 30–35% RH). Patterns are characterized by AFM tapping mode imaging with silicon AFM tips (TAP300Al-G 300 kHz, Budgetsensors).

The effect of protrusion height on the meniscus shape and patterning is investigated through experiments and modeling. The capillary profile at the apex of the tip is modeled using multiphysics finite element analysis software (Comsol Multiphysics) for different probe geometry and different surface wetting conditions. Two-phase flow model for incompressible fluid is used. During the analysis, inertia effects are ignored due to the small volume in the microchannel of the NFP. The results of the analysis summarized in figure 7(*d*) show the evolution of the meniscus at equilibrium for protrusion heights of 200, 400, 600 and 800 nm. The surface wetting conditions are set by the substrate–ink–air of 30, 50 and 90 degrees corresponding to highly hydrophilic, hydrophilic and hydrophobic surfaces.

Modeling results show a ‘flooded tip’ for a protrusion length of 200 nm. The meniscus spreads to the outer shell in each case although the meniscus width varies from 0.95, 0.74 to 0.57 μm for contact angles of 30, 50 and 90 degrees, respectively. Uncontrolled patterning is expected for such writing probes. The meniscus formed by humidity condensation at the tip–substrate interface and the meniscus at the channel opening are connected for protrusion heights

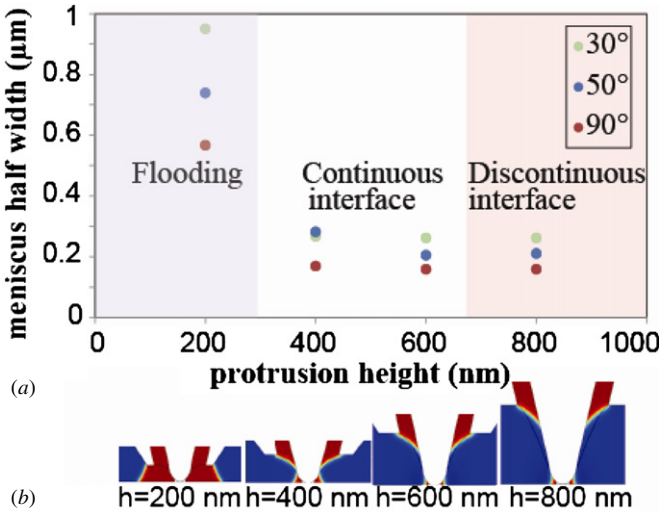

Figure 7. (*a*) Plot shows dependence of the meniscus width at the substrate surface to the protrusion height and the ink–substrate contact angle for hydrophobic (90°), highly hydrophilic (30°) and hydrophilic substrates (50°). (*b*) Meniscus at the tip apex resulting from the modeling of the ink(red)/air(blue)/probe(white) interphase for increasing protrusion height.

of 400 nm as well as 600 nm although the later has only a fine monolayer connecting both interfaces. The meniscus interface becomes discontinuous for protrusion heights of 800 nm.

The modeling results are then compared to experimental patterning results with similar conditions. Probes with protrusion heights of 390, 500, 644 and 1009 nm are identified beforehand by SEM imaging as described earlier. The probes are used to pattern ferritin arrays for increasing dwell time on untreated oxidized substrates. Experiments are repeated three times under nominal conditions while tracking the contact force on each identified probe. The ink-oxide contact angle was characterized by a static sessile drop method at 56° ± 4°. Experimental results shown in figure 8 for different protrusion heights can be partly explained by the meniscus shapes obtained by modeling. A probe with a protrusion height of 390 nm yields very large dots dimensions (~2 μm in diameter) as seen in figure 8(*a*) independent of dwell time which is characteristic of flooded tips (i.e. meniscus spreading to the outer shell) as predicted in prior work [16]. Probes with 500 nm high protrusion lead to dots of increasing diameter with the dual concentration regions as seen in figure 8(*b*): a core with high density of protein surrounded by a monolayer region with randomly dispersed ferritin. Probes with 644 nm high protrusion patterned dots similar to the 500 nm probes although the diameter of the dot core is significantly smaller comparatively (figure 8(*c*)). For a protrusion height of 1009 nm, no pattern was detected indicating that the meniscus forming at the apex of the tip stayed disconnected from the liquid–air interface at the shell preventing the ink diffusion from the tip to the surface.

Sub-100 nm patterning was achieved using probes with 644 nm protrusion height on aged oxidized substrates. The silicon oxide substrates were cleaned and treated by oxygen plasma before aging them in air for seven days. The aging renders the surface highly hydrophobic and limits the meniscus width. Modeling results described in figure 7 predict an increase in the patterning resolution for protrusions above 500 nm and for hydrophobic substrates. Patterns with an increased dwell times of 1, 2 and 3 s, yield uniform dots with heights of 13.8, 28.6 and 58.8 nm and diameters of 34.4, 84.9 and 207.6 nm, respectively (figure 9).

The high-throughput capabilities of the device are tested by patterning with several probes in parallel. Five probes wrote simultaneously an array of 10 × 20 dots (supplementary information available at stacks.iop.org/JMM/23/125014/mmedia). The parallel patterning is repeated five times but shows discrepancy in dot size arising from different contact forces upon each probe. Since the deflection and therefore the contact is monitored by the laser aligned on one probe, any height difference in neighboring probes translate into contact force variations on the substrate surface while writing. The sources contributing to vertical misalignment of the probes were identified and measured. The variation in tip height and cantilever bending was determined to be a minor contribution, estimated at only 0.5 μm by laser interferometry (figure 6(*c*)). However, the sample and/or NFP device tilt induced by mounting in the AFM instrument introduces a significant tilt, which is well-known to produce misprints in DPN array patterning [39].

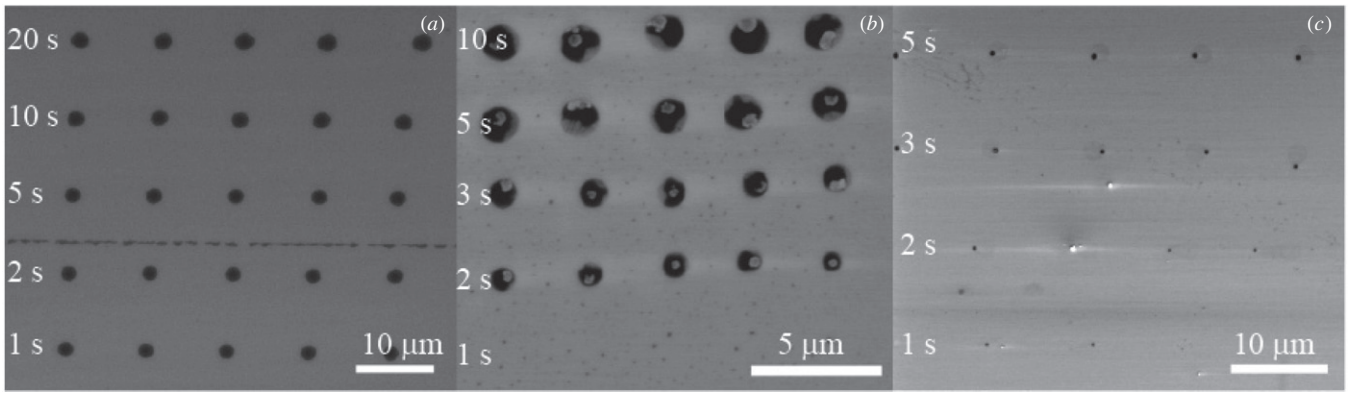

Figure 8. Dependence of the patterning and meniscus shape to the probe protrusion height. SEM images of 5 × 5 dot array of ferritin patterned on an untreated substrate for an increasing protrusion height: (*a*) 390 nm, (*b*) 500 nm, (*c*) 644 nm. Each row of dots corresponds to a specified dwell time from (*a*) 1 to 20 s, (*b*) 1 to 10 s and (*c*) 1 to 5 s, respectively.

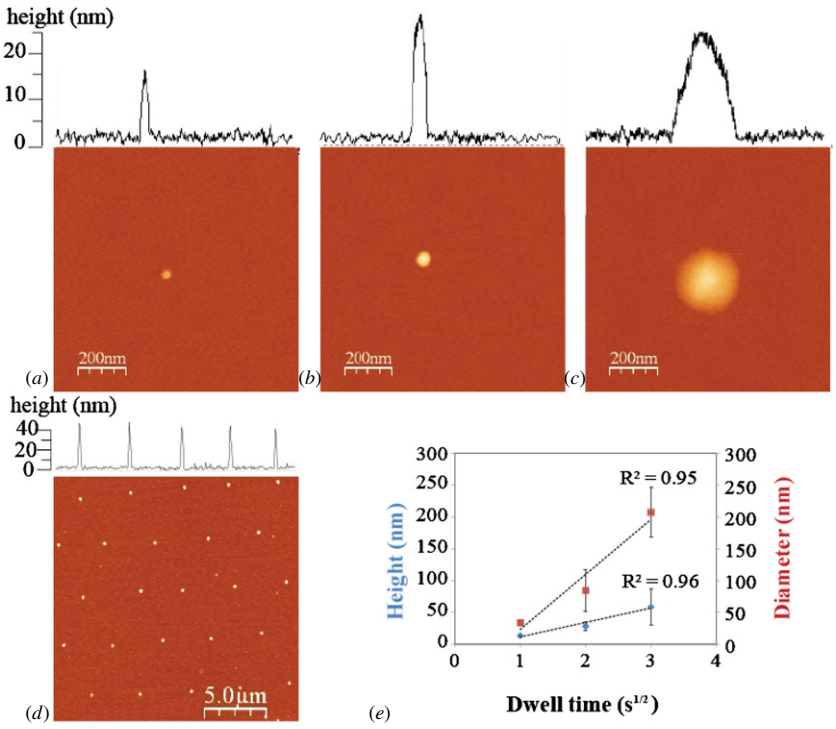

Figure 9. AFM topography images and the corresponding height profiles of ferritin dots patterned by NFP characterized by a protrusion height of 518 nm. (*a*)–(*c*) Dots patterned for increasing dwell time of 1, 2 and 3 s. (*d*) 5 × 5 dot arrays for dwell time of 3 s. Dots have uniform dimensions: 283 ± 19 nm in diameter and 38.5 ± 4.7 nm in height. Height profile of the middle line in the array was acquired in tapping-mode operation. (*e*) Plot of feature size (diameter and height) as a function of the square root of the dwell time along with linear correlation.

The probe-sample relative tilt from one chip extremity to another in the case of our NFP was estimated to vary from 8 to 14 μm by measuring the piezo-tube extension. More accurate strategies such as combining force sensing and 1D/2D leveling discussed elsewhere [29, 42] will be needed to improve contact uniformity between the probes and sample.

5. Conclusions

A fourth generation of NFP was designed and microfabricated, to increase the device structure uniformity across the wafer, and improve patterning reliability. Critical changes in the design and processing steps resulted in an optimized probe geometry that conserves the apex shape and sharpness through the entire fabrication process. Improvements in cantilever bending and channel sealing were demonstrated. These modifications directly impacted the NFP nanopatterning reliability and throughput, by allowing an improved control of the NFP system, including for simultaneous patterning with parallel cantilevers. Control of a higher central core protrusion height through the volcano-shape rim enabled sub-100 nm patterning resolution with one of the critical catalysts (ferritin) not been possible to pattern with using previous NFP generations. The increased reliability of the fourth generation of NFP arrays is expected to enable large scale tip-based nanomanufacturing applications. As a preliminary demonstration, the capabilities of newly fabricated NFP devices were established by patterning arrays of ferritin, an iron-rich protein, on oxidized substrates using parallel probes. Precise parallel assembly of ferritin catalyst at the nanoscale will be applied in future work for integrating *in situ* CVD carbon nanotube synthesis directly on CMOS architecture towards large-scale nanomanufacturing of carbon nanotube-based nanoelectronics.

Acknowledgments

We thank Christina S Miller of the Center for Nanoscale Materials (CNM) at Argonne National Laboratories for the support provided for lithography and etching experiments and Rebecca McNaughton for reviewing structure of the manuscript. HDE acknowledges the support provided by the Nanoscale Science and Engineering Initiative of the National Science Foundation (NSF) under NSF Award EEC-0647560. This work was performed in part at the Center for Nanoscale Materials (CNM), which is supported by the US Department of Energy, Office of Basic Energy Sciences under contract no. DE-AC02-06CH11357, and in part at the fabrication facilities of the Cornell University NanoScale Facility (Ithaca, NY), which is supported by NSF grant ECS-0335765.

References

[1] Zou H W Q 2011 Development of high-throughput control techniques for tip-based nanofabrication *Tip-Based Nanofabrication: Fundamental and Applications* 1st edn ed A Tseng (New York: Springer) pp 325–55
[2] Wang Y, Mirkin C A and Park S-J 2009 Nanofabrication beyond electronics *ACS Nano* **3** 1049–56
[3] Salaita K, Wang Y and Mirkin C A 2007 Applications of dip-pen nanolithography *Nature Nano* **2** 145–55

[4] Tseng A A 2011 Advancements and challenges in development of atomic force microscopy for nanofabrication *Nano Today* **6** 493–509
[5] Morse J 2008 Research challenges for integrated systems nanomanufacturing *Report from the National Science Foundation Workshop* (10 February 2008)
[6] US Office of Science and Technology Policy 2012 A national strategic plan for advanced manufacturing: *Report* (February 2012)
[7] Liddle J A and Gallatin G M Lithography, metrology and nanomanufacturing *Nanoscale* **3** 2679–88
[8] Helmus M N 2006 How to commercialize nanotechnology *Nature Nano* **1** 157–8
[9] Brugger J, Jaecklin V P, Linder C, Blanc N, Indermuhle P F and Rooij N F d 1993 Microfabricated tools for nanoscience *J. Micromech. Microeng.* **3** 161
[10] Anna D 2011 Nanotechnology under the skin *Nanotechnology* **22** 260201
[11] Jones R 2009 Nanotechnology, energy and markets *Nature Nano* **4** 75
[12] Mathur N 2002 Nanotechnology: beyond the silicon roadmap *Nature* **419** 573–5
[13] Kim K-H, Moldovan N and Espinosa H D 2005 A nanofountain probe with sub-100 nm molecular writing resolution *Small* **1** 632–5
[14] Moldovan N, Kim K-H and Espinosa H D 2006 A multi-ink linear array of nanofountain probes *J. Micromech. Microeng.* **16** 1935–42
[15] Kim K H, Sanedrin R G, Ho A M, Lee S W, Moldovan N, Mirkin C A and Espinosa H D 2008 Direct delivery and submicrometer patterning of DNA by a nanofountain probe *Adv. Mater.* **20** 330–4
[16] Loh O Y, Ho A M, Rim J E, Kohli P, Patankar N A and Espinosa H D 2008 Electric field-induced direct delivery of proteins by a nanofountain probe *Proc. Natl Acad. Sci.* **105** 16438–43
[17] Wu B, Ho A, Moldovan N and Espinosa H D 2007 Direct deposition and assembly of gold colloidal particles using a nanofountain probe *Langmuir* **23** 9120–3
[18] Loh O *et al* 2009 Nanofountain-probe-based high-resolution patterning and single-cell injection of functionalized nanodiamonds *Small* **5** 1667–74
[19] Kang W, Yavari F, Minary-Jolandan M, Giraldo-Vela J P, Safi A, McNaughton R L, Parpoil V and Espinosa H D 2013 Nanofountain probe electroporation (NFP-E) of single cells *Nano Lett.* **13** 2448–57
[20] Ginger D S, Zhang H and Mirkin C A 2004 The evolution of Dip-Pen Nanolithography *Angew. Chem. Int. Edn* **43** 30–45
[21] Piner R D, Zhu J, Xu F, Hong S and Mirkin C A 1999 'Dip-Pen' Nanolithography *Science* **283** 661–3
[22] Salaita K, Wang Y, Fragala J, Vega R A, Liu C and Mirkin C A 2006 Massively parallel Dip-Pen Nanolithography with 55000-pen two-dimensional arrays *Angew. Chem. Int. Edn* **45** 7220–3
[23] Weeks B L, Noy A, Miller A E and De Yoreo J J 2002 Effect of dissolution kinetics on feature size in dip-pen nanolithography *Phys. Rev. Lett.* **88** 255505
[24] Pease R F and Chou S Y 2008 Lithography and other patterning techniques for future electronics *Proc. IEEE* **96** 248–70
[25] Gould P 2003 Lithography: rewriting the rules *Mater. Today* **6** 34–9
[26] Gates B D, Xu Q, Love J C, Wolfe D B and Whitesides G M 2004 Unconventional nanofabrication *Annu. Rev. Mater. Rep.* **34** 339–72
[27] Bhushan B (ed) 2010 *Springer Handbook of Nanotechnology* 3rd edn (Berlin: Springer)
[28] Moldovan N, Keun-Ho K and Espinosa H D 2006 Design and fabrication of a novel microfluidic nanoprobe *J. Microelectromech. Syst.* **15** 204–13
[29] Haaheim J *et al* 2010 Self-leveling two-dimensional probe arrays for Dip Pen Nanolithography® *Scanning* **32** 49–59
[30] Seidel H, Csepregi L, Heuberger A and Baumgartel H 1990 Anisotropic etching of crystalline silicon in alkaline solutions *J. Electrochem. Soc.* **137** 3612–26
[31] Prem P, Kazuo S and Sudhir C 2007 Fabrication techniques of convex corners in a (1 0 0)-silicon wafer using bulk micromachining: a review *J. Micromech. Microeng.* **17** R111
[32] Madou M 2002 *Fundamentals of Microfabrication* (Boca Raton, FL: CRC Press)
[33] Schaepkens M, Standaert T E F M, Rueger N R, Sebel P G M, Oehrlein G S and Cook J M 1999 Study of the SiO[sub 2]-to-Si[sub 3]N[sub 4] etch selectivity mechanism in inductively coupled fluorocarbon plasmas and a comparison with the SiO[sub 2]-to-Si mechanism *J. Vac. Sci. Technol.* A **17** 26–37
[34] Oehrlein G S *et al* 1999 Surface science issues in plasma etching *IBM J. Res. Dev.* **43** 181–97
[35] Shul R J *et al* 1998 Comparison of plasma etch techniques for III–V nitrides *Solid-State Electron.* **42** 2259–67
[36] Moldovan N, Kim K H and Espinosa H D 2006 A multi-ink linear array of nanofountain probes *J. Micromech. Microeng.* **16** 1935
[37] Wille H, Burte E and Ryssel H 1992 Simulation of the step coverage for chemical vapor deposited silicon dioxide *J. Appl. Phys.* **71** 3532
[38] Chang L and Yu-Chong T 1999 Sealing of micromachined cavities using chemical vapor deposition methods: characterization and optimization *J. Microelectromech. Syst.* **8** 135–45
[39] Chang C P, Pai C S and Hsieh J J 1990 Ion and chemical radical effects on the step coverage of plasma enhanced chemical vapor deposition tetraethylorthosilicate films *J. Appl. Phys.* **67** 2119
[40] Ohring M 2002 Mechanical properties of thin films *Materials Science of Thin Films* 2nd edn (New York: Academic) pp 711–81
[41] Li Y, Kim W, Zhang Y, Rolandi M, Wang D and Dai H 2001 Growth of single-walled carbon nanotubes from discrete catalytic nanoparticles of various sizes *J. Phys. Chem.* B **105** 11424–31
[42] Huo F, Zheng Z, Zheng G, Giam L R, Zhang H and Mirkin C A 2008 Polymer pen lithography *Science* **321** 1658–60